Correlated interfacial water transport and proton conductivity in perfluorosulfonic acid membranes

Xiao Ling[a], Mischa Bonn[a], Katrin F. Domke[a,1], and Sapun H. Parekh[a,b,1,2]

[a]Department of Molecular Spectroscopy, Max Planck Institute for Polymer Research, D-55128 Mainz, Germany; and [b]Department of Biomedical Engineering, University of Texas at Austin, Austin, TX 78712

Edited by Michael L. Klein, Institute of Computational Molecular Science, Temple University, Philadelphia, PA 19122, and approved March 22, 2019 (received for review October 10, 2018)

Water must be effectively transported and is also essential for maximizing proton conductivity within fuel-cell proton-exchange membranes (PEMs). Therefore, identifying relationships between PEM properties, water transport, and proton conductivity is essential for designing optimal PEMs. Here, we use coherent Raman spectroscopy to quantify real-time, in situ diffusivities of water subspecies, bulk-like and nonbulk-like (interfacial) water, in five different perfluorosulfonic acid (PFSA) PEMs. Although the PEMs were chemically diverse, water transport within them followed the same rule: Total water diffusivity could be represented by a linear combination of the bulk-like and interfacial water diffusivities. Moreover, the diffusivity of interfacial water was consistently larger than that of bulk-like water. These measurements of microscopic transport were combined with through-plane proton conductivity measurements to reveal the correlation between interfacial water transport and proton conductivity. Our results demonstrate the importance of maximizing the diffusivity and fractional contribution of interfacial water to maximize the proton conductivity in PFSA PEMs.

proton-exchange membranes | water transport | confined water | nanoscale chemistry | proton transport

Proton-exchange membranes are the central, performance-limiting component of hydrogen fuel-cell (PEMFC) technology for numerous reasons. A long-standing challenge in large-scale PEMFC implementation concerns water management within PEMs. Water structure and transport are intimately related to PEMFC performance through regulation of water management (i.e., its spatial distribution) and by affecting proton transport within perfluorosulfonic acid (PFSA) PEMs (1–3). Rational development of high-performance PEMs has remained challenging because it requires a fundamental knowledge of the link between membrane chemistry, structure, and transport properties. The current industry standard PEM is Nafion, which consists of hydrophobic Teflon chains with ether-linked side chains that are terminated by hydrophilic sulfonic acid head groups (4). The polymer architecture of Nafion leads to hydrophilic–hydrophobic phase separation, resulting in self-assembly of ionic clusters (domains) of a few nanometers in diameter (4–8).

The understanding of Nafion morphology has largely converged to a view of a hydrophobic membrane matrix containing nanoscale, hydrophilic domains with widths up to 4 nm in diameter (9). Water is believed to reside in the hydrophilic domains and facilitate proton transport through the membrane. The nanoscale width of the domains makes Nafion an intriguing system regarding transport properties because nanoscale confinement may strongly influence the water chemistry and transport in the membrane (10–12). Indeed, vibrational spectroscopy of water—which reflects the local water chemical environment through changes in the shape of OH vibrational bands—in Nafion by different groups has shown that water hydrogen bonding (coordination) is strongly perturbed in Nafion compared with "normal" or bulk water (13–15). More recent work on water properties in nanometer-sized Nafion mimics, sodium bis(2-ethylhexyl)sulfosuccinate (aerosol OT) micelles, by Fayer and coworkers (16, 17), has established the existence of two water species with very different vibrational signatures and dynamics in these micelles: bulk water and interfacial water. The same group has proposed a core–shell model of water structure in confinement where bulk-like water exists at the core of the micelles, and interfacial (shell) water exists at the micelle interface (18). Benziger and coworkers (19, 20) have proposed a similar core–shell model for water structure in Nafion channels, and our previous results have experimentally confirmed the existence of two subspecies of water—bulk-like water (bulkW) and nonbulk-like water (nonbulkW) or interfacial water—in Nafion and similar interfacial geometries (21, 22). That said, the functional implication (if any) of these different water populations on, e.g., transport properties of Nafion is unknown. Previous work by Song et al. (23) using pulsed field gradient NMR spectroscopy with different spin labels has suggested that water near the hydrophobic portion of Nafion exhibits much faster diffusivity (more than four orders of magnitude larger) than bulkW in Nafion, but the relationship between these diffusivities and overall water transport is not clear. Moreover, a recent study using NMR, neutron scattering, and simulations showed a somewhat contradictory result: subdiffusive transport of water confined to ionic domains in various PFSA PEMs, including Nafion and Aquivion membranes (24). It has, in summary, been challenging to experimentally address the

Significance

Fuel-cell proton-exchange membranes (PEMs) are central to hydrogen fuel-cell technology. The mechanism and optimization of proton transport in these materials is intimately linked with hydration and water transport. Studies of water transport in PEMs have previously been limited to macroscopic permeability measurements. Our work connects the macroscopic proton transport in PEMs to the molecular water arrangement: Two distinct types of water, differing in their degree of molecular coordination, transit the membrane at very different rates. The more weakly coordinated water species consistently exhibits faster transit across five different PEMs and shows a direct correlation to the proton conductivity, suggesting that designing PEMs to maximize the fraction of undercoordinated water is key for maximizing overall transport.

Author contributions: X.L., K.F.D., and S.H.P. designed research; X.L. performed research; X.L., M.B., and S.H.P. contributed new reagents/analytic tools; X.L., M.B., K.F.D., and S.H.P. analyzed data; and X.L., M.B., K.F.D., and S.H.P. wrote the paper.

The authors declare no conflict of interest.

This article is a PNAS Direct Submission.

[1]K.F.D. and S.H.P. contributed equally to this work.

[2]To whom correspondence should be addressed. Email: sparekh@utexas.edu.

This article contains supporting information online at www.pnas.org/lookup/suppl/doi:10.1073/pnas.1817470116/-/DCSupplemental.

Published online April 15, 2019.

combined effect of PFSA architecture and water structure (and dynamics) on water and proton transport properties of these media.

Computational work has arguably more successfully targeted the transport mechanisms and relation between water and proton transport in PFSA PEMs (reviewed in refs. 25 and 26). An important quality of these theoretical studies is the derived mechanistic insight into the proton transport mechanism for differing hydration and polymer structure. In particular, reactive multistate empirical valence band (MS-EVB) simulations have shown that the two primary mechanisms for proton transport, the Grotthuss proton-hopping mechanism (or structural diffusion) and vehicular diffusion are anticorrelated to some degree in the confined PSFA geometry compared to bulk water where the two mechanisms appear to be additive (27, 28). The anticorrelation makes it more difficult to distinguish between the contributions of the Grotthuss and vehicular components. Further simulations by Voth and coworkers (29) that included the complete Grotthuss physics using reactive dynamics with MS-EVB went on to show that the sulfonic acid-to-sulfonic acid hydration shell proton-transfer mechanism is dominant in the PFSA geometry. The authors showed that excess protons at hydration levels of 5, 9, and 12 were almost always (95% of the time) within two water solvation shells of at least one acidic head group, which themselves have overlapping solvation shells that facilitate Grotthuss-type proton transport in PFSA nanoconfined water pools. Increasing the hydration level changes the size and connectivity of the hydration layers of the sulfonic acids; however, increased hydration does not lead to a significant increase of the hydrated protons in the center (or core) of a water pool beyond two hydration shells from sulfonic acid groups. This suggests that sulfonic-acid-assisted passing of protons is the dominant mechanism for proton transport, even at higher hydration levels, in contrast to previous work using an empirical, nonreactive force field that showed that high-speed proton transport in PFSAs was reminiscent of transport in bulk water (30). In that study, the authors found that high-speed proton transport occurred predominantly in the core of PFSA PEM channels—presumably much farther away from sulfonic acid groups—at high hydration levels because strong proton interaction with sulfonic acid groups could slow transport (30). Interestingly, the width and geometry of the water layer drastically changed the proton solvation and overall water structure as well (31). An overview of the literature shows that while numerous simulations have largely clarified how protons transport in nanoconfined PFSA materials, the relation between water—or water subspecies—transport and proton transport has not experimentally been demonstrated.

Vibrational spectroscopy is an effective method to identify water subspecies in situ; however, measuring molecular transport properties in real time in a microscopic volume is experimentally demanding. Here, we present real-time, in situ, label-free measurement of water and water subspecies diffusion in fully hydrated (saturating λ-condition) PEMs using broadband coherent anti-Stokes Raman scattering (BCARS) spectroscopy. We study five different PEMs, differing in chemical composition and processing and show that the apparent diffusion coefficient (ADC) for nonbulkW (interfacial water) is always larger than that of bulkW. By combining our vibrational spectroscopy with macroscale ac impedance measurements of through-plane conductivity under the same conditions, we found that the diffusivity of nonbulkW was directly correlated with proton conductivity in PFSA PEMs, independent of membrane chemistry.

Results

H_2O–D_2O Exchange Experiments with PFSA Membranes. We measured in situ, time-dependent water transport in Nafion and other PFSA membranes using a microfluidic Y valve to initiate H_2O–D_2O exchange within an immobilized PFSA membrane in our BCARS microscope, as in our previous work (21). BCARS is a nonlinear analog of Raman spectroscopy that provides a quantitative Raman-like (RL) vibrational spectrum (700–4,000 cm^{-1}), after appropriate processing (*SI Appendix, Experimental Methods*), with millisecond time resolution from a femtoliter volume in the sample. Fig. 1 (*Top Left*) shows a schematic of the measurement wherein a PFSA membrane, in this case, dispersion cast Nafion 212 (N212, equivalent weight = 1,100 g mol^{-1}), was initially saturated by D_2O, representing a D_2O-equilibrated state. After switching the Y valve to initiate exchange, BCARS spectra from the membrane were acquired at 100-ms intervals. Switching the microfluidic channel solution to H_2O took ∼5 s in our gravity-driven, laminar flow conditions (*SI Appendix*, Fig. S1), after which H_2O diffused into the membrane and D_2O in membrane diffused out (Movie S1).

The OH and OD concentrations were obtained from the integrated amplitudes of the OH (2,918–3,810 cm^{-1}) and OD (2,182–2,780 cm^{-1}) stretching vibrations, respectively (Fig. 1*B*). The time-dependent OH and OD concentrations show that the diffusion process in N212 was complete within ∼30 s of initially detecting the OH signal. Fitting the time-dependent OH and OD traces with an analytical solution to Fick's second law (see *SI Appendix*, Fig. S2 and Eq. **S3** for fitting details), allowed us to quantify the transport by extracting an ADC from the traces. The ADC for the integrated OH amplitude [ADC(OH) = 3.75 ± 0.10 × 10^{-10} m^2/s (mean ± SD)] was statistically identical to the ADC of the integrated OD amplitude [ADC(OD) = 3.89 ± 0.20 × 10^{-10} m^2/s (mean ± SD)] in N212 (*SI Appendix*, Fig. S3) from n = 6 independent N212 samples. These numbers are quantitatively consistent with our previous measurements using a slightly modified experimental and fitting protocol (21) and are consistent with other values reported for water diffusion in Nafion

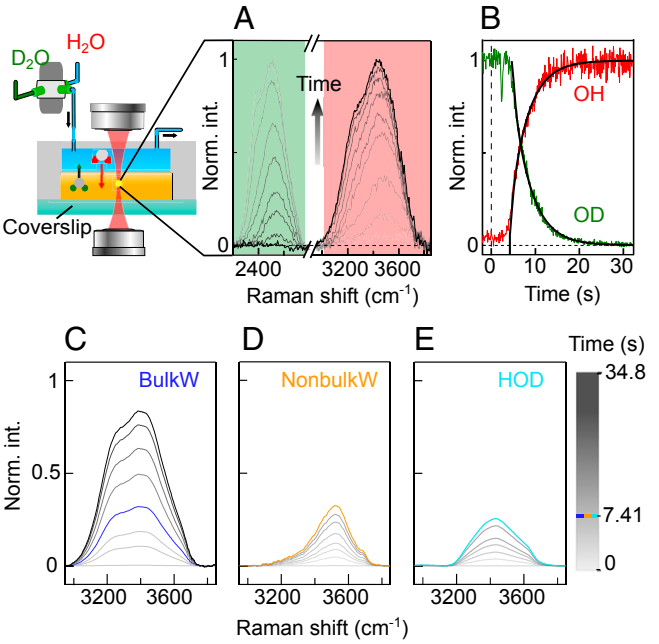

Fig. 1. Measuring water transport in situ in PFSA membranes using real-time vibrational microscopy. (*A*) RL intensity of the OD-stretching vibration (green) decreases while the intensity of the OH-stretching vibration (red) increases during the H_2O–D_2O exchange. All RL spectra were normalized to the maximum value in the respective regions. (*B*) OD (green) and OH (red) concentrations vs. time obtained by integrating the respective spectral regions; solid black lines are fits to the Fickian diffusion model described in *SI Appendix*. The concentration profiles were normalized to their maximum value. (*C*–*E*) Time-dependent spectral amplitudes showing water subspecies contributions during H_2O–D_2O exchange in N212. All spectra are divided by the maximum of the OH band at t = 30 s (after exchange is complete) to show different temporal evolution.

(*SI Appendix*, Table S1). Moreover, the reverse experiment—D_2O diffusing in an H_2O equilibrated membrane—shows statistically identical results (*SI Appendix*, Fig. S3), which confirms that OH and OD exchange simultaneously. Accordingly, both the OH and OD regions can, in principle, be used to analyze the diffusivity of water in Nafion; however, for simplicity, we focus on the OH region for experiments of H_2O diffusing into a D_2O-equilibrated membrane for the remainder of this work. Finally, we note that experiments from different depths (relative to the channel–membrane interface) and lateral positions within N212 showed that ADC(OH) was not position dependent (*SI Appendix*, Figs. S2 and S3), as expected for a nanoporous membrane that is uniform over micrometer length scales (the size of our focal volume).

Quantifying Heterogeneous Diffusivity of Water in PFSA Membranes. We have previously shown that the overall OH-stretch intensity of water in Nafion can be decomposed into two subspecies contributions: bulkW and (nonbulkW). BulkW is represented by the RL response of MilliQ water, and the nonbulkW spectrum was deduced by analyzing many RL spectra of two different Nafion membranes at multiple hydration states (*SI Appendix*, Fig. S4) with a constrained classical least-squares (CCLS) global fitting algorithm (see *SI Appendix*, Fig. S5 for fitting details). Inspection of the nonbulkW shape (*SI Appendix*, Fig. S5, orange) shows that it is clearly less hydrogen-bonded compared with bulkW with the main peak being strongly blue-shifted to higher frequency.

In addition to bulkW and nonbulkW subspecies, exchange of D_2O for H_2O will necessarily result in an intermediate HOD species, with a distinct vibrational response, which also contributes to the OH-stretch intensity (32–34). Therefore, to analyze the shape of the time-dependent RL spectra, a third spectral component for HOD is required. We deduced the HOD RL spectrum using the CCLS algorithm on RL spectra from a series of D_2O/H_2O mixtures (*SI Appendix*, Figs. S6 and S7). Using the deduced HOD lineshape, the fitted concentration of H_2O, D_2O, and HOD from the mixtures was quantitatively consistent with those predicted by the established binomial mixing for isotopic scrambling (*SI Appendix*, Fig. S8) (33, 34), confirming the accuracy of the HOD lineshape. In principle, one would expect a bulk and nonbulk HOD subspecies for Nafion, and therefore, we further checked whether the binomial mixing held for H_2O, D_2O, and HOD in N212 equilibrated in different H_2O/D_2O mixtures using the deduced HOD lineshape. Also here, good agreement was observed between the decomposition concentrations, in this case using bulkW, nonbulkW, and HOD lineshapes, and those predicted by the binomial mixing rule (*SI Appendix*, Fig. S9). These results show that the OH-stretch vibrational band in Nafion during H_2O–D_2O exchange can be described in a consistent manner using the sum of three lineshapes: bulkW, nonbulkW, and HOD.

With spectral shapes for the primary water subspecies in the membrane, we could further determine their respective diffusivities. Time-dependent RL spectra of H_2O–D_2O exchange in N212 were decomposed using nonnegative least-squares according to $S_{meas} = C_{bulkW} \times S_{bulkW} + C_{nonbulkW} \times S_{nonbulkW} + C_{HOD} \times S_{HOD} + E$, where S_{meas} is the experimental RL spectrum, C_X is the fractional concentration of subspecies X, S_X is the subspecies X RL spectrum, and E is the error between the experimental and calculated spectrum. The time-dependent contributions of the different components to the overall OH-region spectra from N212 during the H_2O–D_2O exchange are shown in Fig. 1 *C*–*E*. Notably, the nonbulkW (and HOD) component reached its maximum value much earlier (at t = 7.4 s) than bulkW (~35 s), demonstrating the larger mobility of the nonbulkW water species. Fig. 2*A* shows the C vs. t curves for each subspecies in N212 from all RL spectra in a representative exchange experiment. The residuals from these decompositions (Fig. 2*A*, *Insets*, gray curves) are less than 5% of the total spectral amplitude, and adding a fourth component to the decomposition did not improve the fit (*SI Appendix*, Figs. S10 and S11). Fig. 2*A* confirms the observation that nonbulkW (orange) appears earlier (at t ~ 3 s) than bulkW (dark blue at t ~ 7 s) in N212. The concentration of HOD (light blue) at first increases with the appearance of nonbulkW and decreases to zero upon complete exchange, as expected, since it is a transient species that should disappear as the membrane completely exchanges D_2O for H_2O. Similar water transport was observed in three individual experiments within one N212 membrane and across n = 6 different N212 membrane samples.

Before analyzing the concentration profiles of the subspecies with the 1D diffusion model, we performed a control experiment to verify that the isotopic scrambling reaction $H_2O + D_2O \rightleftharpoons 2HOD$ was sufficiently fast to not influence our measurements on the millisecond timescale. We measured H_2O diffusion into a 4.2-mm-deep × 1-mm-wide D_2O-filled aperture (*SI Appendix*,

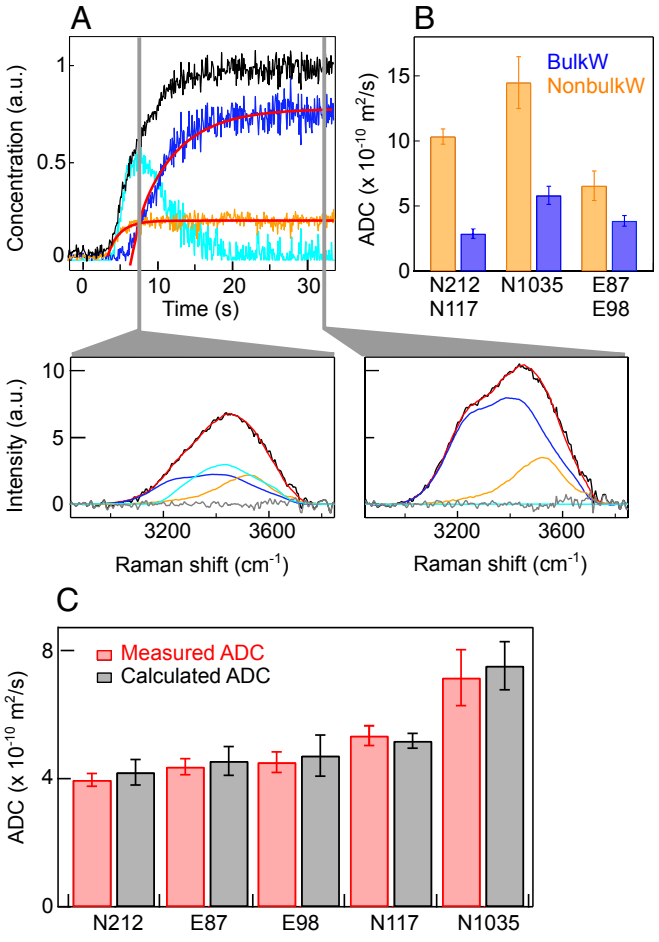

Fig. 2. Heterogeneous water transport in PFSA membranes. (*A*) Decomposed concentration profiles of bulkW (blue), nonbulkW (orange), and HOD (cyan) (see *SI Appendix*, section 6 for decomposition details) in N212 during H_2O–D_2O exchange; the total normalized OH signal is shown in black. Red lines show fits to 1D Fickian model for bulkW and nonbulkW. (*A*, *Bottom*) Measured RL spectra (black) and fitted spectra (red) at times indicated by gray vertical lines. RL spectra of subspecies of bulkW (blue), nonbulkW (orange), and HOD (blue), as well as residuals (gray), are shown in the spectral plots. (*B*) ADC of bulkW (blue) and nonbulkW (orange) computed from fitting concentration profiles for different PFSA membranes. Error bars are SDs of the ADCs from three measurements in each of n = 6 independent membrane pieces for each PFSA PEM. (*C*) Total water (OH) diffusivity in PFSA membranes is a linear combination of bulkW and nonbulkW ADCs. Measured values (red bars) and calculated values (gray bars) as a linear combination of ADC(bulkW) and ADC(nonbulkW) weighted by their fractional concentration in the respective membrane under H_2O-saturated conditions.

Fig. S12), decomposed the time-dependent OH region RL spectra into HOD and bulkW, and calculated the ADC(bulkW) from the 1D Fickian model (*SI Appendix*, Eq. **S3**). Should isotopic exchange strongly influence the bulkW signal we detect, one would expect our ADC analysis considering only diffusion (as opposed to reaction–diffusion) to disagree strongly with the mutual diffusion coefficient of water. We found an ADC(bulkW) ~2.2 ± 0.4 × 10^{-9} m^2/s (n = 3 independent experiments) from this experiment, which is nearly identical to the accepted H_2O mutual diffusion constant (D_{H2O} ~ 2.3 × 10^{-9} m^2/s) reported in experimental and theoretical studies (35–39). This close agreement demonstrates that our diffusion-only analysis accurately captures the H_2O/D_2O transport phenomena in the exchange experiments. Thus, the 1D Fickian diffusion model was used to calculate the ADC of bulkW and nonbulkW from their respective concentration profiles.

We found that ADC(bulkW) = 2.5 ± 0.3 × 10^{-10} m^2/s and ADC(nonbulkW) = 10.1 ± 0.9 × 10^{-10} m^2/s (mean ± SD), respectively, from n = 6 independent N212 samples. To determine how membrane properties such as equivalent weight (EW) or polymer architecture influence water transport, H_2O–D_2O exchange experiments were conducted in various other PFSA-based membranes: Nafion 117 (N117), Nafion 1035 (N1035), Aquivion E87 (E87), and Aquivion E98 (E98) membranes. N117 is formed from the chemically identical polymer (EW = 1,100 g mol^{-1}) as N212 but is processed using melt extrusion. The extrusion processing results in different physical properties such as membrane thickness, ionic channel size, water–membrane interaction, and proton conductivity as reported previously (21, 40, 41). N1035 (EW = 1,000 g mol^{-1}), also extrusion processed, contains more SO_3H-terminated head groups per gram of polymer compared with N117. Aquivion E87 (EW = 870 g mol^{-1}) and E98 (EW = 980 g mol^{-1}) are also extrusion processed but have a different polymer architecture from Nafion-based membranes as their side chains are shorter.

The RL spectra from H_2O–D_2O exchange experiments on the fully hydrated PFSAs were decomposed similarly as those from N212 with the same spectral shapes for bulkW, nonbulkW, and HOD. This was justified given the good agreement between the static H_2O hydrated spectra of each membrane and the spectral fits (*SI Appendix*, Fig. S13). The extracted ADC(bulkW) and ADC(nonbulkW) of N117 were 2.8 ± 0.6 × 10^{-10} m^2/s and 10.4 ± 0.3 × 10^{-10} m^2/s (n = 6 independent N117 samples), respectively—statistically identical to those measured in N212 (see *SI Appendix*, Fig. S14*A* for statistics). The subspecies diffusivities measured in E87 and E98 (*SI Appendix*, Fig. S14*B*) were also equivalent: ADC(bulkW) = 3.9 ± 0.4 × 10^{-10} m^2/s and ADC(nonbulkW) = 6.6 ± 1.3 × 10^{-10} m^2/s (n = 6 independent E87 and E98 samples). N1035 exhibited the fastest diffusivity among all of the PFSA membranes, and the ADC(bulkW) and ADC(nonbulk) of it were 5.8 ± 0.7 × 10^{-10} m^2/s and 14.5 ± 2.0 × 10^{-10} m^2/s (n = 7 independent experiments), respectively (Fig. 2*B*).

The overall water diffusivity—ADC(OH)—in N1035 was (statistically) significantly faster by 1.8-fold compared with N212, E87, and E98 (Fig. 2*C*, red bars and *SI Appendix*, Fig. S3) and by 1.3-fold compared with N117. We previously proposed that the sum of the ADCs for bulkW and nonbulkW weighted by their respective fractional concentration in the membrane (when fully hydrated with H_2O) could reproduce the measured ADC(OH) (21). From the fractional concentration of each subspecies at long times after exchange (effectively an equilibrium H_2O state), we indeed found that a weighted sum of the ADC(bulkW) and ADC(nonbulkW), ADC(OH)' = C_{bulkW} × ADC(bulkW) + $C_{nonbulkW}$ × ADC(nonbulk), where C_X was the fractional concentration of species X at equilibrium in H_2O, almost perfectly reproduced the total measured ADC(OH) in all five PFSA samples (Fig. 2*C*, gray bars).

NonbulkW Transport and Membrane Proton Conduction Are Correlated. The overall water transport is determined by physical properties of a membrane: porosity, tortuosity, and size of ionic domains, which in turn are collectively determined by the chemical structure of the PFSA polymer and the membrane processing method (21, 30, 42, 43). Changing EW and polymer side-chain architecture of PEMs resulted in different porosities, different degrees of water uptake for each of the membranes (*SI Appendix*, Table S2), and varying fractional amounts of bulkW and nonbulkW (*SI Appendix*, Fig. S15). Excluding N212, which was the only membrane processed via drop casting, the total ADC(OH) of the extruded membranes (E87, E98, N1035, and N117) was linearly related to the ADC(nonbulkW), despite the different polymer chemistries and fractional contributions of bulkW and nonbulkW in the different membranes (Fig. 3*A*). This result demonstrates that the overall water transport can be tuned by changing the diffusivity of nonbulkW; the same is not true for bulkW (*SI Appendix*, Fig. S16*A*).

To determine how water transport is related to the functional property of PFSAs: proton conductivity, we measured the through-plane conductivity of the membranes in the fully hydrated state (analogous to our water transport measurements) using AC impedance spectroscopy with a custom-built cell (see *SI Appendix*, Figs. S17–S20 and Table S3 for experimental details, raw impedance data, and model fits). Fig. 3*B* shows the through-plane proton conductivity versus the total ADC(OH) for each PEM and demonstrates that these variables are clearly correlated—again surprisingly independent of the differences in membrane chemistry. Faster water diffusivity facilitates increased proton conductivity, and, because of the linear correlation between ADC(OH) and ADC(nonbulkW), the diffusivity of nonbulkW appears to be fundamentally linked to through-plane proton conductivity in PFSAs.

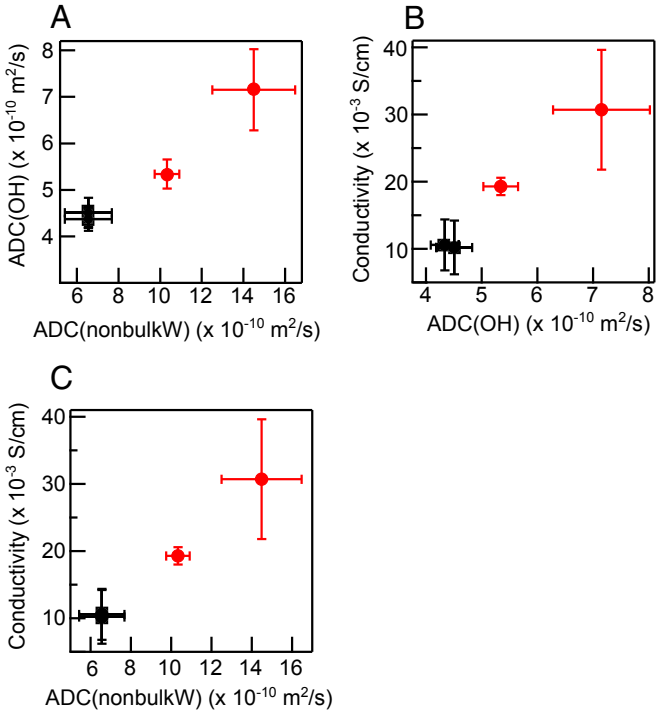

Fig. 3. Linear correlations between ADC(OH) and (*A*) ADC(nonbulkW), (*B*) through-plane proton conductivity; (*C*) linear correlation between ADC (nonbulkW) and through-plane proton conductivity. Black, extruded Aquivion membranes with short side chains; red, extruded Nafion-based membranes with long side chains.

Discussion

Time-lapsed vibrational spectra during H_2O–D_2O exchange were used to quantify the water and water subspecies diffusivity by analysis of the change of the OH-stretching vibration. The overall water diffusivity in PFSA membranes was found to be ~10-fold slower than water transport in bulkW, consistent with previous measurements of water diffusivity in PFSA membranes determined by other methods (*SI Appendix*, Table S1) (19, 44–47). The 10-fold discrepancy between the overall water diffusivity in membranes versus water diffusivity in water is likely to occur because of the physical barriers in the material: the tortuosity (or connectivity) and constrictions of ionic domains (48).

Looking closely at fractional concentrations of water subspecies during the H_2O–D_2O exchange experiments (Fig. 2*A* and *SI Appendix*, Fig. S13 *E–H*), one sees that the [bulkW]/[nonbulkW] ratio was substantially reduced compared with the infinite-time (equilibrium) situation for all PFSA membranes measured. Such a long-lived nonequilibrium (5–7 s in Fig. 2*A*) suggests a physical separation of nonbulkW and bulkW. If the two types of water coexisted within the same ionic domain, one would expect exchange dynamics between these populations after more than 100–1,000 ps (18). This would lead to instantaneous equilibration on our (millisecond) measurement timescale and effectively indistinguishable ADC for both bulkW and nonbulkW, which is not observed experimentally (Fig. 2*B*). Further support for physical separation of bulkW and nonbulkW is provided by the accurate calculation of the ADC(OH) by ADC(OH)′—a weighted linear combination of ADC(nonbulkW) and ADC(bulkW) by the amount of each subspecies in each respective membrane, which indicates that the subspecies transit the membrane as essentially independent entities.

The finding that nonbulkW exhibits faster transport than bulkW in all investigated PFSAs (Fig. 2*B*) is qualitatively similar to that seen previously (even in Nafion membranes), showing that "slippery" water exhibits faster diffusivity than bulkW (49, 50). Closer inspection of the nonbulkW spectral shape shows that, indeed, it exhibits slippery features. The main peak is strongly blue-shifted and narrower relative to that of bulkW (Fig. 2*A*, blue and orange spectra), demonstrating it is clearly less strongly hydrogen bonded (and less coupled) to other water molecules compared with bulkW (51, 52). Together with the previous argument that nonbulkW is physically separate from bulkW, we propose that nonbulkW is the dominant species in smaller ionic channels, where the ability for water molecules to hydrogen bond to other water molecules is reduced, while bulkW is dominant in larger channels or clusters (Fig. 4). This assignment is consistent with coarse-grained, Monte Carlo dissipative particle dynamics simulations (53) that quantitatively reproduced the measured water diffusion coefficients and work by Feng et al. (31) showing diffusion rates strongly depend on confinement geometry.

The observed faster ADC of nonbulkW could arise from two possible mechanisms: (*i*) the network of channels containing nonbulkW is always less tortuous than the bulkW, i.e., in all five PEMs we tested or (*ii*) nonbulkW, being confined in small ionic channels, diffuses by a different transport mechanism, as has been suggested for water in highly confined geometries. Water transport in confined geometries is proposed to occur via water wires (or clusters) that exhibit lower barriers to hydrogen-bond breaking and water rotation compared with bulkW due to water molecules in the wire (cluster) having fewer hydrogen bonds on average (54). The (subnanometer) diameter of narrow ionic channels in PFSAs meets the criterion to confine water on the same scale, so such a transport mechanism is certainly plausible.

The model in Fig. 4, with narrow channels containing the faster-diffusing nonbulkW, combined with the data in Fig. 3 showing correlated nonbulkW transport and proton conductivity, has potential implications for the proton transport mechanism in PFSA materials. Specifically, our results and model are consistent with the mechanism for proton transport in PFSAs proposed by Savage et al. (29): Narrow channels will facilitate passing hydrated protons from head group to head group via confined nonbulkW with high efficiency. Interestingly, the larger diffusion coefficient of water in the narrow channels could further contribute to the proton mobility by increasing the vehicular proton diffusion since vehicular proton diffusion is purportedly correlated with vehicular water diffusion. As the size of the water-containing structures shrinks in PFSA PEMs, these structures will contain more (faster-diffusing) nonbulkW, which should also enhance vehicular proton transport.

Independent of the exact mechanism responsible for accelerated transport of water and protons in confined channels, experimental evidence has demonstrated that transport of both species increases in confinement (55, 56). A thorough study where one can explicitly vary head group density [similar to that simulated by Jang et al. (57)] and channel width independently is necessary to disambiguate these effects for PFSA transport.

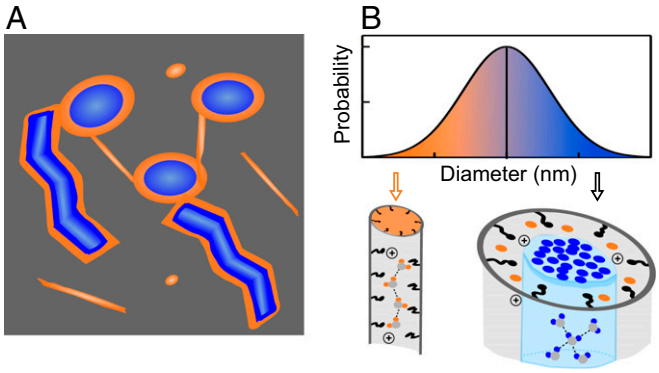

Fig. 4. Model for ionic domains in PFSAs showing how nonbulkW and bulkW can contribute to overall water transport and still exhibit distinct diffusivities. (*A*) Smaller ionic water channels contain only nonbulkW (orange) and larger ionic water clusters and channels are dominated by bulkW (blue). (*B*, *Bottom*) Schematic showing the structure and binding of water in large versus small ionic water domains. BulkW (blue) is the primary species in larger domains while smaller domains contain mainly nonbulkW (orange). BulkW maintains interactions characteristic of bulkW while nonbulkW forms a less-coordinated water network confined by the polymer (gray and black) in the smaller domains.

Conclusion

Water transport in PFSA PEMs is heterogeneous, with chemically unique water subspecies exhibiting surprisingly distinct diffusivities. By measuring transport in real time and spectrally distinguishing the water subspecies, we observed that the weaker-coordinated, interfacial water subspecies exhibited significantly larger mobility than the bulkW water in all PFSA membranes investigated, suggesting that weakly hydrogen-bonded water always diffuses faster than bulkW water in PFSA materials. The overall water diffusivity in PFSA membranes can be quantitatively described by a linear combination of the bulk-like and nonbulk-like diffusivities weighted by the corresponding fractional amount of each species. Finally, we show that the functional property of PFSA membranes—proton conductivity—is directly linked with nonbulk-like, interfacial water transport. Our work highlights the connection of the nanoscale channel architecture (channel connectivity/tortuosity) and water confinement on the transport properties of PFSA PEMs. Therefore, we believe that future PFSA designs that maximize the amount of nonbulk-like (by, e.g., producing a larger fraction of smaller ionic channels at the expense of larger domains) and maximize its diffusivity (by increasing porosity via membrane chemistry and production) will yield the highest proton conductivity PEMs.

Methods

Nafion 117 (183 μm thick, 360 g m^{-2}; DuPont), Nafion 212 (50.8 μm thick, 100 g m^{-2}; DuPont), Nafion 1035 (89 μm thick, 175 g m^2; Chemours), Aquivion E87 – 05S (50 μm thick, 1.93 g cm^3; Solvay), and Aquivion E98 – 05 (50 μm thick, 1.93 g cm^3; Solvay) were used in this work. Further experimental and analytical methods for CARS spectroscopy and microscopy are described in *SI Appendix, Experimental Methods*.

ACKNOWLEDGMENTS. We gratefully acknowledge A. Hanewald, A. Kaltbeitzal, U. Zhumaev, M. J. Van Zadel, F. Fleissner, N. Billecke, Y. Nagata, and J. Hunger for technical support and scientific discussions. K.F.D. acknowledges support through the Emmy Noether program of the German Research Foundation (DFG) DO 1691/1-1 and through the "Plus 3" program of the Boehringer Ingelheim Foundation. X.L. and K.F.D. acknowledge funding through European Union 7th Framework Programme (Grant ITN-FINON 607842). S.H.P. acknowledges funding from the DFG Grant PA 252611-1 Marie Curie Foundation CIG322284.

1. Kreuer KD (2001) On the development of proton conducting polymer membranes for hydrogen and methanol fuel cells. *J Membr Sci* 185:29–39.
2. Kunimatsu K, Bae B, Miyatake K, Uchida H, Watanabe M (2011) ATR-FTIR study of water in Nafion membrane combined with proton conductivity measurements during hydration/dehydration cycle. *J Phys Chem B* 115:4315–4321.
3. Buie CR, et al. (2006) Water management in proton exchange membrane fuel cells using integrated electroosmotic pumping. *J Power Sources* 161:191–202.
4. Gierke TD, Munn GE, Wilson FC (1981) The morphology in Nafion perfluorinated membrane products, as determined by wide-angle and small-angle X-ray studies. *J Polym Sci Pol Phys* 19:1687–1704.
5. Kim MH, Glinka CJ, Grot SA, Grot WG (2006) SANS study of the effects of water vapor sorption on the nanoscale structure of perfluorinated sulfonic acid (NAFION) membranes. *Macromolecules* 39:4775–4787.
6. Kusoglu A, Cho KT, Prato RA, Weber AZ (2013) Structural and transport properties of Nafion in hydrobromic-acid solutions. *Solid State Ion* 252:68–74.
7. Kusoglu A, Modestino MA, Hexemer A, Segalman RA, Weber AZ (2012) Subsecond morphological changes in Nafion during water uptake detected by small-angle X-ray scattering. *ACS Macro Lett* 1:33–36.
8. Schmidt-Rohr K, Chen Q (2008) Parallel cylindrical water nanochannels in Nafion fuel-cell membranes. *Nat Mater* 7:75–83.
9. Devanathan R (2008) Recent developments in proton exchange membranes for fuel cells. *Energy Environ Sci* 1:101–119.
10. Hummer G, Rasaiah JC, Noworyta JP (2001) Water conduction through the hydrophobic channel of a carbon nanotube. *Nature* 414:188–190.
11. Falk K, Sedlmeier F, Joly L, Netz RR, Bocquet L (2010) Molecular origin of fast water transport in carbon nanotube membranes: Superlubricity versus curvature dependent friction. *Nano Lett* 10:4067–4073.
12. Berezhkovskii A, Hummer G (2002) Single-file transport of water molecules through a carbon nanotube. *Phys Rev Lett* 89:064503.
13. Falk M (1980) An infrared study of water in perfluorosulfonate (Nafion) membranes. *Can J Chem* 58:1495–1501.
14. Basnayake R, Peterson GR, Casadonte DJ, Jr, Korzeniewski C (2006) Hydration and interfacial water in Nafion membrane probed by transmission infrared spectroscopy. *J Phys Chem B* 110:23938–23943.
15. Liu S, Aquino AJA, Korzeniewski C (2013) Water-ionomer interfacial interactions investigated by infrared spectroscopy and computational methods. *Langmuir* 29:13890–13897.
16. Spry DB, Goun A, Glusac K, Moilanen DE, Fayer MD (2007) Proton transport and the water environment in nafion fuel cell membranes and AOT reverse micelles. *J Am Chem Soc* 129:8122–8130.
17. Moilanen DE, Fenn EE, Wong D, Fayer MD (2009) Water dynamics at the interface in AOT reverse micelles. *J Phys Chem B* 113:8560–8568.
18. Fayer MD, Levinger NE (2010) Analysis of water in confined geometries and at interfaces. *Annu Rev Anal Chem (Palo Alto Calif)* 3:89–107.
19. Zhao Q, Majsztrik P, Benziger J (2011) Diffusion and interfacial transport of water in Nafion. *J Phys Chem B* 115:2717–2727.
20. Majsztrik PW, Satterfield MB, Bocarsly AB, Benziger JB (2007) Water sorption, desorption and transport in Nafion membranes. *J Membr Sci* 301:93–106.
21. Ling X, Bonn M, Parekh SH, Domke KF (2016) Nanoscale distribution of sulfonic acid groups determines structure and binding of water in Nafion membranes. *Angew Chem Int Ed Engl* 55:4011–4015.
22. Moreno Ostertag L, Ling X, Domke KF, Parekh SH, Valtiner M (2018) Characterizing the hydrophobic-to-hydrophilic transition of electrolyte structuring in proton exchange membrane mimicking surfaces. *Phys Chem Chem Phys* 20:11722–11729.
23. Song J, Han OH, Han S (2015) Nanometer-scale water- and proton-diffusion heterogeneities across water channels in polymer electrolyte membranes. *Angew Chem Int Ed Engl* 54:3615–3620.
24. Berrod Q, Hanot S, Guillermo A, Mossa S, Lyonnard S (2017) Water sub-diffusion in membranes for fuel cells. *Sci Rep* 7:8326.
25. Dreßler C, Kabbe G, Sebastiani D (2016) Insight from atomistic simulations of protonation dynamics at the nanoscale. *Fuel Cells (Weinh)* 16:682–694.
26. Arntsen C, Savage J, Tse Y-LS, Voth GA (2016) Simulation of proton transport in proton exchange membranes with reactive molecular dynamics. *Fuel Cells (Weinh)* 16:695–703.
27. Feng S, Voth GA (2011) Proton solvation and transport in hydrated nafion. *J Phys Chem B* 115:5903–5912.
28. Petersen MK, Voth GA (2006) Characterization of the solvation and transport of the hydrated proton in the perfluorosulfonic acid membrane nafion. *J Phys Chem B* 110:18594–18600.
29. Savage J, Tse Y-LS, Voth GA (2014) Proton transport mechanism of perfluorosulfonic acid membranes. *J Phys Chem C* 118:17436–17445.
30. Karo J, Aabloo A, Thomas JO, Brandell D (2010) Molecular dynamics modeling of proton transport in nafion and hyflon nanostructures. *J Phys Chem B* 114:6056–6064.
31. Feng S, Savage J, Voth GA (2012) Effects of polymer morphology on proton solvation and transport in proton-exchange membranes. *J Phys Chem C* 116:19104–19116.
32. Walrafen GE (1968) Raman spectral studies of HDO in H_2O. *J Chem Phys* 48:244–251.
33. Libnau FO, Christy AA, Kvalheim OM (1995) Determination of the equilibrium constant and resolution of the HOD spectrum by alternating least-squares and infrared analysis. *Appl Spectrosc* 49:1431–1437.
34. Max J-J, Chapados C (2002) Isotope effects in liquid water by infrared spectroscopy. *J Chem Phys* 116:4626–4642.
35. Longsworth LG (1960) The mutual diffusion of light and heavy water. *J Phys Chem* 64:1914–1917.
36. Mills R (1973) Self-diffusion in normal and heavy water in the range 1-45.deg. *J Phys Chem* 77:685–688.
37. Dahal U, Adhikari NP (2012) Molecular dynamics study of diffusion of heavy water in normal water at different temperatures. *J Mol Liq* 167:34–39.
38. Izvekov S, Voth GA (2002) Car-Parrinello molecular dynamics simulation of liquid water: New results. *J Chem Phys* 116:10372–10376.
39. Wang JH, Robinson CV, Edelman IS (1953) Self-diffusion and structure of liquid water. III. Measurement of the self-diffusion of liquid water with H^2, H^3 and O^{18} as Tracers[1]. *J Am Chem Soc* 75:466–470.
40. The Chemours Company (2016) Nafion Membranes N115,N117,N1110 Datasheet. Available at https://www.chemours.com/Nafion/en_US/assets/downloads/nafion-extrusion-cast-membranes-product-information.pdf. Accessed April 10, 2019.
41. Fuel Cell Earth. Nafion Membranes NR211 and NR212 Datasheet. Available at fuelcellearth.com/pdf/NRE-211_212.pdf. Accessed April 10, 2019.
42. Ding C, et al. (2013) Morphology and electrochemical properties of perfluorosulfonic acid ionomers for vanadium flow battery applications: Effect of side-chain length. *ChemSusChem* 6:1262–1269.
43. Brandell D, Karo J, Liivat A, Thomas JO (2007) Molecular dynamics studies of the Nafion, Dow and Aciplex fuel-cell polymer membrane systems. *J Mol Model* 13:1039–1046.
44. Every HA, Hickner MA, McGrath JE, Zawodzinski TA (2005) An NMR study of methanol diffusion in polymer electrolyte fuel cell membranes. *J Membr Sci* 250:183–188.
45. Zawodzinski TA, et al. (1993) Water uptake by and transport through Nafion 117 membranes. *J Electrochem Soc* 140:1041–1047.
46. Suresh G, Scindia Y, Pandey A, Goswami A (2005) Self-diffusion coefficient of water in Nafion-117 membrane with different monovalent counterions: A radiotracer study. *J Membr Sci* 250:39–45.
47. Hallinan DT, Elabd YA (2009) Diffusion of water in Nafion using time-resolved Fourier transform infrared–attenuated total reflectance spectroscopy. *J Phys Chem B* 113:4257–4266.
48. Berrod Q, et al. (2015) Nanostructure and transport properties of proton conducting self-assembled perfluorinated surfactants: A bottom-up approach toward PFSA fuel cell membranes. *Macromolecules* 48:6166–6176.
49. Ho TA, Papavassiliou DV, Lee LL, Striolo A (2011) Liquid water can slip on a hydrophilic surface. *Proc Natl Acad Sci USA* 108:16170–16175.
50. Sendner C, Horinek D, Bocquet L, Netz RR (2009) Interfacial water at hydrophobic and hydrophilic surfaces: Slip, viscosity, and diffusion. *Langmuir* 25:10768–10781.
51. Holmes NC, Nellis WJ, Graham WB, Walrafen GE (1985) Spontaneous Raman scattering from shocked water. *Phys Rev Lett* 55:2433–2436.
52. Corcelli SA, Skinner JL (2005) Infrared and Raman line shapes of dilute HOD in liquid H_2O and D_2O from 10 to 90 degrees C. *J Phys Chem A* 109:6154–6165.
53. Dorenbos G, Suga Y (2009) Simulation of equivalent weight dependence of Nafion morphologies and predicted trends regarding water diffusion. *J Membr Sci* 330:5–20.
54. Kalra A, Garde S, Hummer G (2003) Osmotic water transport through carbon nanotube membranes. *Proc Natl Acad Sci USA* 100:10175–10180.
55. Tunuguntla RH, Allen FI, Kim K, Belliveau A, Noy A (2016) Ultrafast proton transport in sub-1-nm diameter carbon nanotube porins. *Nat Nanotechnol* 11:639–644.
56. Tunuguntla RH, et al. (2017) Enhanced water permeability and tunable ion selectivity in subnanometer carbon nanotube porins. *Science* 357:792–796.
57. Jang SS, Molinero V, Çağın T, Goddard WA (2004) Nanophase-segregation and transport in Nafion 117 from molecular dynamics simulations: Effect of monomeric sequence. *J Phys Chem B* 108:3149–3157.